The Role of Ephaptic Coupling and Gap Junctional Coupling in Modulating the Initiation and Dynamics of Reentrant Arrhythmias

Ning Wei[1,*], Elena G. Tolkacheva[2]
1: Department of Mathematics, Purdue University
150 N. University St, West Lafayette, IN 47907.
2: Department of Biomedical Engineering, University of Minnesota
312 Church St SE, Minneapolis, MN 55455
Corresponding author *: wei307@purdue.edu (N. Wei).

Abstract

Cardiac myocytes synchronize through electrical signaling to contract heart muscles, facilitated by gap junctions (GJs) located in the intercalated disc (ID). GJs provide low-resistance pathways for electrical impulse propagation between myocytes, considered the primary mechanism for electrical communication in the heart. However, research indicates that conduction can persist without GJs. Ephaptic coupling (EpC), which depends on electrical fields in the narrow ID between adjacent myocytes, offers an alternative mechanism for cardiac conduction when GJs are impaired. Research suggests that EpC can enhance conduction velocity (CV) and reduce the likelihood of conduction block (CB), particularly when GJs are impaired, demonstrating the anti-arrhythmic potential of EpC. Reduced GJ communication increases the susceptibility of heart to arrhythmias due to ectopic or triggered activity, highlighting the pro-arrhythmic effect of gap junctional uncoupling. However, the interplay between GJs and EpC, and their roles in the initiation, dynamics, and termination of arrhythmias, remain unclear. Reentry, characterized by a loop of electrical activity, is a common mechanism underlying arrhythmogenesis in the heart. This study aims to explore the interplay between EpC and GJ on reentry initiation and its underlying dynamics. Specifically, we employed a two-dimensional (2D) discrete bidomain model that integrates EpC to simulate ephaptic conduction during reentry. We quantitatively assessed the outcomes of reentry initiation and the resulting dynamics across different levels of EpC, GJs, and initial perturbations. The results show that sufficiently strong EpC (narrow clefts) tends to suppress the initiation of reentry, leading to nonsustained or absent reentrant activity, while also introducing instability and heterogeneity into the cardiac dynamics. In contrast, relatively weak EpC (wide clefts) support sustained reentry with a stable rotor. Furthermore, we found that sufficiently strong EpC can lower the maximal dominant frequency observed during reentrant activity. Overall, this suggests that strong EpC exerts an anti-arrhythmic effect.

Keywords: Ephaptic coupling, gap junctions, reentry, cardiac dynamics, conduction velocity, dominant frequency.

1 Introduction

Cardiac myocytes synchronize to contract the heart muscles, facilitating blood circulation through electrical signaling. Gap junctions (GJs), located in the intercalated disc (ID) act as low-resistance pathways facilitating electrical connections between cardiac myocytes, thereby enabling the propagation of electrical impulses [2, 3, 26, 30]. GJ is widely recognized as the primary mechanism for electrical communication between myocytes [24]. However, recent experimental findings have raised concerns regarding whether conduction in the heart can be sustained without GJs [7, 37]. For example, mice with GJ knockout [37] still exhibit electrical propagation in the heart, albeit with discontinuous and slow conduction. Remarkably, these mice can survive for up to two months, suggesting the existence of alternative mechanisms for cell-to-cell communication in the heart.

Ephaptic coupling (EpC) serves as an alternative mechanism for cardiac conduction when GJs are dysfunctional. Studies have shown that EpC relies heavily on the electrical fields within the narrow clefts between neighboring myocytes [27, 28]. Since the middle of 20th century, EpC has undergone extensive experimental and numerical investigations, yet direct experimental evidence for its existence remains elusive. Consequently, efforts have been

made to indirectly demonstrate the presence of EpC by studying its physiological role in the heart under various conditions [6, 8, 9, 13, 16, 17, 21, 27, 29, 31, 33–35]. For example, research indicates that EpC can assist in restoring cardiac conduction when GJ is impaired by enhancing conduction velocity (CV) [8, 11, 12, 16, 17, 33] and mitigating conduction block (CB) [33].

Reduced gap junctional communication can make the heart more susceptible to ectopic or triggered activity from afterdepolarizations, thus contributing to arrhythmias [10, 15, 24]. GJs are significantly reduced during myocardial ischemia, a state where reduced blood flow to the heart muscle leads to insufficient oxygen supply. Ischemic condition disrupts normal electrical activity of the heart, increasing the likelihood of arrhythmias. We demonstrated that EpC of sufficient strength (with a sufficiently small cleft width, d_{cleft}) can significantly diminish conduction failure across the ischemic tissue [34], suggesting a beneficial effect of EpC on arrhythmogenesis in the ischemic heart. We also demonstrated that sufficiently strong EpC terminates reentry in healthy and ischemic heart [35]. Reentry is a primary mechanism underlying arrhythmogenesis in the heart, including atrial fibrillation and ventricular tachycardia. Despite these advancements, the interplay between EpC and GJs on the initiation, dynamics, and termination of cardiac arrhythmias remains elusive.

The electrophysiological properties of cardiac tissue, such as CV, refractoriness, and excitability, are key factors influencing arrhythmic dynamics, particularly the spatio-temporal behavior of electrical activity in the heart. Understanding reentry initiation and its underlying dynamics is essential for improving the treatment and management of cardiac arrhythmias. The goal of this study is to explore how different levels of EpC and GJs influence the initiation and dynamics of reentry, utilizing a two-dimensional (2D) discrete bidomain model of EpC. Specifically, we quantitatively assessed the incidence of reentry initiation and analyzed the subsequent dynamics across different levels of EpC, GJs, and initial perturbations. The results show that sufficiently strong EpC (narrow clefts) tends to suppress the initiation of reentry, leading to nonsustained or absent reentrant activity, while also introducing instability and heterogeneity into the cardiac dynamics. In contrast, relatively weak EpC (wide clefts) supports sustained reentry with a stable rotor. Furthermore, we found that sufficiently strong EpC can lower the maximal dominant frequency (max DF) observed during reentrant activity. Overall, this suggests that strong EpC exerts an anti-arrhythmic effect.

2 Materials and Methods

2.1 2D model overview. We employed our previously developed 2D discrete bidomain model with EpC [33–35] to simulate cardiac conduction, which is strongly influenced by the junctional cleft space between neighboring cells. In this model, each cell is represented as a cylinder, and the cells are interconnected via gap junctions to form an $M \times N$ rectangular lattice. At each lattice point (i, j), both the intracellular potential, $\phi_i^{(i,j)}$, and the extracellular potential, $\phi_e^{(i,j)}$, are defined. The junctional cleft is positioned between adjacent cells (i, j) and $(i, j+1)$, and we introduced a cleft potential, $\phi_c^{(i,j+\frac{1}{2})}$, at the location $(i, j+\frac{1}{2})$. The region adjacent to the cleft, which lies within the extracellular region, is called the extracellular-cleft space, with its potential denoted as $\phi_{ec}^{(i,j+\frac{1}{2})}$.

The top panel of Fig. 1 in [33] shows the lattice view of the model, while the bottom panel provides a circuit diagram representing two adjacent cells connected through the shared cleft space and end-to-end gap junctions (GJ_{end}). Note that side-to-side gap junctions (GJ_{side}) and the resistive connection (R_{ee}) between extracellular spaces in the transverse direction are not included. The cleft space is modeled as a narrow compartment with resistive connections (R_c) to the extracellular-cleft space, and the resistive connections between the extracellular and extracellular-cleft spaces are represented by R_{ec}. The intracellular and extracellular spaces of each cell are separated by the side membrane, while the intracellular and cleft spaces are separated by the end membrane. These side and end membranes function independently, allowing for the flow of ionic and capacitive currents. To simplify the computations, we assume that the intracellular and extracellular spaces of each cell are isopotential.

2.2 Modeling EpC. EpC is critically dependent on the presence of a cleft space between the ends of adjacent cells, which communicates with the end membranes of neighboring cells and the extracellular space independently. To model EpC, we derived an equation for the cleft space based on the principle of current conservation. This equation incorporates the balance of capacitive and ionic currents across the end membranes of two adjacent cells sharing a common cleft potential, as well as the resistive current flowing from the cleft into the extracellular space, characterized

by R_c. The current balance is captured by the following expression:

$$-A_{\text{end}}C_m\frac{\partial(\phi_i^{(i,j)}-\phi_{\text{c}}^{(i,j+\frac{1}{2})})}{\partial t}-A_{\text{end}}C_m\frac{\partial(\phi_i^{(i,j+1)}-\phi_{\text{c}}^{(i,j+\frac{1}{2})})}{\partial t}-I_{\text{end}} + \frac{\phi_c^{(i,j+\frac{1}{2})}-\phi_{ec}^{(i,j+\frac{1}{2})}}{R_c}=0. \tag{1}$$

R_c is inversely proportional to the cleft width (d_{cleft}), with the relevant formulas available in [12, 33]. We chose d_{cleft} values of 8 nm, 15 nm, 20 nm, and 35 nm [33–35] to represent varying strengths of EpC. Notably, a smaller d_{cleft} corresponds to higher R_c, indicating a stronger EpC effect. A d_{cleft} of 115 nm indicates a negligible EpC effect.

The model equations were derived using current balance principles for the intracellular, extracellular, cleft, and extracellular-cleft spaces. Specifically, the current balance captures the equilibrium among capacitive, ionic, and resistive currents across the different domains. The detailed equations are presented in Eqs. (2.1) to (2.4) of our previous publication [33], and all model parameters are provided in Table 1 of Ref. [33].

2.3 Membrane dynamics. To model the dynamics of excitable cells in normal tissue, we used the Luo-Rudy dynamic model 2007 (LRd2007), which is specific to guinea pig ventricular tissue [18]. In our 2D model, we localized the fast sodium (INa) channels to the end membrane, as observed in experimental studies [4, 5, 19]. This localization was achieved by redistributing the INa channels across the end membrane, while maintaining a constant total number of ionic channels or conductance. Other ionic channels are uniformly distributed across both the side and end membranes, with the channels and their gating variables functioning independently on each membrane.

2.4 Analysis of reentry dynamics. Our goal is to thoroughly examine the effects of EpC and GJ on reentry initiation and the resulting dynamics. To accomplish this, we employed different levels of GJs at 100%, 80%, 50%, 30%, and 10% of the nominal value (666 mS/cm^2 [33]), along with varying levels of EpC. Additionally, for each combination of GJ and EpC, we introduced $\pm$10% and $\pm$20% perturbations from the steady state to the initial conditions of the potentials, ionic concentrations, and gating variables of all ionic currents.

We quantitatively evaluated reentry initiation outcomes, categorizing them as sustained reentry, nonsustained reentry, or no reentry. Additionally, we calculated the DF, max DF, and the number of DF regions (# DF regions) in the 2D lattice. In the context of arrhythmia, DF represents the frequency of the highest peak in the power spectrum of cardiac electrical activity, reflecting the primary frequency of reentrant circuits or other rapid drivers in the heart. DF is calculated by applying the fast Fourier transform (FFT) to the voltage signals generated by our 2D model. It is widely used to characterize arrhythmia dynamics [1, 23, 36] and plays a crucial role in assessing the pro- or anti-arrhythmic effects of EpC. The max DF corresponds to the highest frequency detected at a specific site in the time series, identifying regions with the most rapid reentrant or focal sources. The # DF regions reflects the spatial complexity of reentry, with a higher count suggesting more fragmented and potentially unstable reentrant pathways. Together, these metrics offer a comprehensive evaluation of the stability, speed, and spatial organization of reentrant arrhythmias under varying conditions.

2.5 Numerical simulations. Numerical simulations were performed on a $M \times N$ lattice ($M = N = 550$) with a total simulation duration of 1200 ms. Each cell had a length of 0.01 cm and a radius of 0.0011 cm, with a time step of 0.01 ms. To initiate reentry, we applied an S1-S2 cross-field stimulation protocol. The initial stimulus (S1) was delivered to the left boundary of the lattice at time $(t) = 0$, with an amplitude of 0.15 μA and a duration of 2 ms. Following this, the second stimulus (S2) was administered to the bottom of the lattice at the S1-S2 interval, while preserving the same amplitude and duration. To minimize the impact of the pacing protocol on reentry dynamics, we maintained a consistent S1-S2 interval (140 ms) across different levels of EpC, GJ and initial perturbations.

To solve the system, we used a splitting method, which enabled us to update the potential, ionic concentrations, and gating variables of ion channels independently. Specifically, we handled the linear components of the system using the backward Euler method, while linearizing the nonlinear components (such as ionic currents and dynamics) around the values from the previous time step, and then managing them with the same method. The system was solved using

a direct method, specifically the backslash operator in Matlab. The wavefront of typical action potential propagation is identified as the point in space where the lateral transmembrane potential (V_m) exceeds -30 mV, accompanied by a positive temporal derivative ($\frac{\partial V_m}{\partial t} > 0$). Activation was monitored by determining the earliest activation time (EAT) at each column of the $M \times N$ lattice. Longitudinal conduction velocity (CV_L) was calculated using linear regression of the EAT across 20–80% of the lattice length to minimize boundary effects.

3 Results

3.1 The impact of EpC on reentry dynamics. We first induced reentry in our 2D model using the cross-field pacing protocol with an S1-S2 interval of 140 ms, with steady-state as the initial setup. The values of d_{cleft} were set to 15 nm and 115 nm, with GJs kept at 100%. Top panels of Figs. 1 and 2 present snapshots of V_m at different time points, illustrating nonsustained and sustained reentry in the presence ($d_{\text{cleft}} = 15$ nm) and absence ($d_{\text{cleft}} = 115$ nm) of EpC, respectively. The bottom panels of both figures display representative V_m traces at points A, B, C and D along with the corresponding DF values.

As illustrated in the top panel of Fig. 1, the reentry dissipates over time and is not sustained in the presence of EpC. Conversely, the top panel of Fig. 2 demonstrates a stable and persistent reentrant pattern in the near absence of EpC. As indicated in the bottom panel of both figures, the V_m traces for points A and C, located at the center of the reentry, exhibit chaotic behavior, while the V_m traces for points B and D, situated at the periphery of the reentry, display a rapid yet regular pattern. It's important to note that the DFs calculated from voltage traces at points A and C are lower compared to those at points B and D. The center of reentry has a smaller DF compared to the periphery due to the nature of the electrical activity in these regions. At the center of the reentrant circuit, the wavefront is constantly turning, leading to more complex and slower conduction patterns, which reduces the DF. In contrast, the periphery experiences faster and more regular conduction, resulting in a higher DF. This difference is driven by the dynamics of wavefront propagation and the curvature of the reentrant pathway, which is more pronounced at the center. Comparing Fig. 1 with Fig. 2, one can suggest that EpC can reduce DF. Consequently, with strong EpC, DF may not reach the level needed for sustained reentry, indicating that EpC can suppress the initiation of reentry.

Fig. 3 presents 2D DF maps for Figs. 1 and 2, where reentry is nonsustained and sustained, respectively. It is evident that the max DF is considerably lower for nonsustained reentry (8 Hz, left) compared to sustained reentry (13 Hz, right). However, the number of regions in the DF map is greater for nonsustained reentry (6 regions, left) than for sustained reentry (3 regions, right).

Fig. 4 presents the 2D DF maps for $d_{\text{cleft}} = 15$ nm, 20 nm, 35 nm, and 115 nm with 100% GJ coupling. Reentry did not occur at $d_{\text{cleft}} = 8$ nm; therefore, its corresponding DF map is not shown. Notably, reentry is nonsustained for $d_{\text{cleft}} = 15$ nm and 20 nm, whereas sustained reentry is observed at 35 nm and 115 nm. This suggests that stronger EpC (i.e., smaller d_{cleft}) suppresses the initiation of reentry. To further understand the impact of EpC on the dynamics of reentry, we examined the max DF and the # DF regions across the 2D lattice. The results indicate that the max DF increases with larger d_{cleft}, while the # DF regions shows a biphasic trend—first increasing and then decreasing with d_{cleft} —with a peak observed at $d_{\text{cleft}} = 20$ nm. These findings suggest that EpC reduces the max DF and exerts a dual influence on the spatial complexity of reentry.

3.2 Impact of EpC and GJs on reentry initiation and subsequent dynamics. To thoroughly investigate the effects of EpC and GJs on reentry initiation and the resulting dynamics, we assessed outcomes across a range of EpC levels, GJs, and initial perturbations. Reentry initiation was categorized as sustained (red), nonsustained (blue), or absent (black), as summarized in Table 1. The results indicate that smaller d_{cleft} values are more likely to result in nonsustained or no reentry, while wider clefts tend to promote sustained reentry, regardless of the level of GJs and initial perturbation. In particular, at $d_{\text{cleft}} = 8$nm, nearly all cases result in either nonsustained reentry or no reentry. In contrast, sustained reentry consistently occurs when EpC was minimal ($d_{\text{cleft}} = 115$ nm). Additionally, reduced GJs increased the probability of both nonsustained and sustained reentry across all d_{cleft} values. The results above demonstrate that strong EpC suppresses reentry initiation, indicating an anti-arrhythmic effect.

We next examined cardiac dynamics both prior to and following the onset of reentry. Specifically, we investigated how EpC and GJ coupling influence CV_L before reentry develops, as illustrated in Fig. 5. As shown in the figure, CV_L

decreases as EpC becomes stronger (i.e., as d_{cleft} decreases), regardless of the level of GJs. Additionally, we investigated the max DF (Fig. 6) and the # DF regions (Fig. 7) across different levels of EpC, GJ, and initial perturbations, as outlined in Table 1, for both nonsustained and sustained reentry events. As shown in Fig. 6, max DF decreases as d_{cleft} decreases. While there are slight variations in the trend depending on the perturbations and GJs, the overall trend remains consistent. This suggests that EpC has the potential to lower the max DF, indicating an anti-arrhythmic effect of EpC. In contrast, the # DF regions shows a nonlinear response to variations in d_{cleft}, peaking at $d_{\text{cleft}} = 15$ nm or 20 nm—indicative of moderate EpC strength. This suggests that although moderate EpC may suppress the initiation of reentry, it can also give rise to more fragmented electrical activity. Moreover, while sustained reentry is rarely observed at $d_{\text{cleft}} = 8$ nm, negative initial perturbations at this level of EpC result in more fragmented activity, suggesting that the inhibition of reentry initiation may take longer to fully manifest. Table 2 summarizes the locations of peaks in the # DF regions as a function of d_{cleft}, across varying GJ levels and initial condition perturbations. Peaks shown in red and blue correspond to sustained and non-sustained reentry, respectively. Although peaks appear at different values of d_{cleft}, they are predominantly associated with non-sustained reentry. In summary, a sufficiently narrow cleft may prevent the initiation of reentry, but also cause the wavefront of reentry to meander around the tissue, this introduces instability and heterogeneity in the cardiac dynamics, leading to different electrochemical properties in various parts of the tissue. However, at a wider cleft, reentry is sustained and the rotor center remains stable.

4 Discussion

The impact of EpC on cardiac arrhythmias is a topic of great significance from both scientific and clinical perspectives. Exploring the effects of EpC in this direction holds considerable importance. Our study [35] demonstrates that EpC can terminate reentry under both normal and ischemic conditions. However, the mechanisms underlying this termination, as well as the influence of EpC on the initiation and dynamics of reentry, remain unclear. Our current research focuses on analyzing the dynamics of reentry using DF. DF, max DF, and the # DF regions offer quantitative metrics to assess the frequency distribution and spatial organization of cardiac electrical signals. DF reflects the predominant frequency of electrical activity in cardiac tissue, with higher DFs indicating increased arrhythmogenic potential and a propensity for sustained arrhythmias [22, 25, 38]. Elevated max DFs correlate with heightened excitability and an increased likelihood of arrhythmia initiation, particularly in regions prone to ectopic activity or conduction abnormalities [20]. Similarly, a greater number of regions with high DFs indicates widespread electrical instability and a higher risk of arrhythmia propagation and maintenance [14, 32]. Understanding these parameters individually provides crucial insights into different aspects of arrhythmogenesis, facilitating targeted therapeutic interventions and risk stratification in clinical practice.

There is a close relationship among EpC, max DF, and the number of regions in the DF map. As the cleft size decreases (and EpC increases), resistance to ion flow increases, affecting the conduction dynamics and stability of reentrant circuits. Specifically, a reduction in d_{cleft} can lead to a longer refractory period and conduction delays or CB, which affect the formation and timing of reentry, thereby disrupting the circular pathway required for sustained reentry. In particular, when $d_{\text{cleft}} = 15$ nm and 20 nm, the reentrant circuit can still initiate depolarization, but it encounters tissue that has already been activated and is in a refractory state, allowing the activity to persist longer before eventually dissipating. DF act as indicators of the rate of electrical excitation. Higher DFs are often associated with increased electrical instability, enhancing the potential for reentry circuits to form. In addition, a larger number of regions in the DF map indicates fragmented conduction, signifying reentry instability. From this perspective, EpC is closely related to both DF and the number of regions in the DF maps.

The mathematical model employed in this study possesses several limitations. Specifically, our model overlooks intricate details such as the precise cell geometry, including any offsets, as well as the microdomain effects within the extracellular space and the intricate geometry of the intercalated discs. While these factors could be crucial for understanding reentry dynamics, incorporating them all would substantially escalate the computational demands of our large-scale 2D simulation. Consequently, this poses a significant challenge to our numerical investigations. However, addressing these aspects remains a focus of our future endeavors.

5 Conclusion

The goal of this study is to explore how different levels of EpC and GJs influence the initiation and dynamics of

reentry, utilizing a 2D discrete bidomain model of EpC. Specifically, we quantitatively assessed the outcomes of reentry initiation and the resulting dynamics across different levels of EpC, GJs, and initial perturbations. The results show that sufficiently strong EpC (narrow clefts) tends to suppress the initiation of reentry, leading to nonsustained or absent reentrant activity, while also introducing instability and heterogeneity into the cardiac dynamics. In contrast, relatively weak EpC (wide clefts) supports sustained reentry with a stable rotor. Furthermore, we found that sufficiently strong EpC can lower the max DF observed during reentrant activity. Overall, this suggests that strong EpC exerts an anti-arrhythmic effect.

6 Author Contributions

Ning Wei designed the numerical experiments and ran the numerical simulation; Ning Wei and Elena G. Tolkacheva analyzed the results; Ning Wei and Elena G. Tolkacheva wrote and edited the manuscript.

References

[1] Felipe Atienza and José Jalife. Reentry and atrial fibrillation. *Heart Rhythm*, 4(3):S13–S16, 2007.

[2] Philippe Beauchamp, Cécile Choby, Thomas Desplantez, Karin de Peyer, Karen Green, Kathryn A Yamada, Robert Weingart, Jeffrey E Saffitz, and André G Kléber. Electrical propagation in synthetic ventricular myocyte strands from germline connexin43 knockout mice. *Circ. Res.*, 95(2):170–178, 2004.

[3] Philippe Beauchamp, Thomas Desplantez, Megan L McCain, Weihui Li, Angeliki Asimaki, Ghislaine Rigoli, Kevin Kit Parker, Jeffrey E Saffitz, and Andre G Kleber. Electrical coupling and propagation in engineered ventricular myocardium with heterogeneous expression of connexin43. *Circulation research*, 110(11):1445–1453, 2012.

[4] Sidney A Cohen. Immunocytochemical localization of rh1 sodium channel in adult rat heart atria and ventricle presence in terminal intercalated disks. *Circulation*, 94(12):3083–3086, 1996.

[5] Sidney A Cohen and Linda K Levitt. Partial characterization of the rh1 sodium channel protein from rat heart using subtype-specific antibodies. *Circulation Research*, 73(4):735–742, 1993.

[6] Elizabeth D Copene and James P Keener. Ephaptic coupling of cardiac cells through the junctional electric potential. *J. Math. Biol.*, 57(2):265–284, 2008.

[7] Stephan B Danik, Fangyu Liu, Jie Zhang, H Jacqueline Suk, Gregory E Morley, Glenn I Fishman, and David E Gutstein. Modulation of cardiac gap junction expression and arrhythmic susceptibility. *Circ. Res.*, 95(10):1035–1041, 2004.

[8] Sharon A George, Mohammad Bonakdar, Michael Zeitz, Rafael V Davalos, James W Smyth, and Steven Poelzing. Extracellular sodium dependence of the conduction velocity-calcium relationship: evidence of ephaptic self-attenuation. *American Journal of Physiology-Heart and Circulatory Physiology*, 310(9):H1129–H1139, 2016.

[9] Sharon A George, Gregory Hoeker, Patrick J Calhoun, Michael Entz, Tristan B Raisch, D Ryan King, Momina Khan, Chandra Baker, Robert G Gourdie, James W Smyth, Morten S Nielsen, and Steven Poelzing. Modulating cardiac conduction during metabolic ischemia with perfusate sodium and calcium in guinea pig hearts. *American Journal of Physiology-Heart and Circulatory Physiology*, 316(4):H849–H861, 2019.

[10] David E Gutstein, Gregory E Morley, Houman Tamaddon, Dhananjay Vaidya, Michael D Schneider, Ju Chen, Kenneth R Chien, Heidi Stuhlmann, and Glenn I Fishman. Conduction slowing and sudden arrhythmic death in mice with cardiac-restricted inactivation of connexin43. *Circ. Res.*, 88(3):333–339, 2001.

[11] Paul E Hand, Boyce E Griffith, and Charles S Peskin. Deriving macroscopic myocardial conductivities by homogenization of microscopic models. *Bull. Math. Biol.*, 71(7):1707–1726, 2009.

[12] Paul E Hand and Charles S Peskin. Homogenization of an electrophysiological model for a strand of cardiac myocytes with gap-junctional and electric-field coupling. *Bull. Math. Biol.*, 72(6):1408–1424, 2010.

[13] Gregory S Hoeker, Carissa C James, Allison N Tegge, Robert G Gourdie, James W Smyth, and Steven Poelzing. Attenuating loss of cardiac conduction during no-flow ischemia through changes in perfusate sodium and calcium. *American Journal of Physiology-Heart and Circulatory Physiology*, 319(2):H396–H409, 2020.

[14] Jérôme Kalifa, Kazuhiko Tanaka, Alexey V Zaitsev, Mark Warren, Ravi Vaidyanathan, David Auerbach, Sandeep Pandit, Karen L Vikstrom, Robert Ploutz-Snyder, Arkadzi Talkachou, et al. Mechanisms of wave fractionation at boundaries of high-frequency excitation in the posterior left atrium of the isolated sheep heart during atrial fibrillation. *Circulation*, 113(5):626–633, 2006.

[15] Jan P Kucera, André G Kléber, and Stephan Rohr. Slow conduction in cardiac tissue, ii: effects of branching tissue geometry. *Circulation research*, 83(8):795–805, 1998.

[16] James Lin and James P Keener. Ephaptic coupling in cardiac myocytes. *IEEE Trans.Biomed.Eng.*, 60(2):576–582, 2013.

[17] Joyce Lin and James P Keener. Modeling electrical activity of myocardial cells incorporating the effects of ephaptic coupling. *Proc.Natl. Acad. Sci.*, 107(49):20935–20940, 2010.

[18] Leonid M Livshitz and Yoram Rudy. Regulation of ca2+ and electrical alternans in cardiac myocytes: role of camkii and repolarizing currents. *American Journal of Physiology-Heart and Circulatory Physiology*, 292(6):H2854–H2866, 2007.

[19] Sebastian KG Maier, Ruth E Westenbroek, Kenneth A Schenkman, Eric O Feigl, Todd Scheuer, and William A Catterall. An unexpected role for brain-type sodium channels in coupling of cell surface depolarization to contraction in the heart. *Proc. Natl. Acad. Sci.*, 99(6):4073–4078, 2002.

[20] Raphael P Martins, Kuljeet Kaur, Elliot Hwang, Rafael J Ramirez, B Cicero Willis, David Filgueiras-Rama, Steven R Ennis, Yoshio Takemoto, Daniela Ponce-Balbuena, Manuel Zarzoso, et al. Dominant frequency increase rate predicts transition from paroxysmal to long-term persistent atrial fibrillation. *Circulation*, 129(14):1472–1482, 2014.

[21] Yoichiro Mori, Glenn I Fishman, and Charles S Peskin. Ephaptic conduction in a cardiac strand model with 3d electrodiffusion. *Proc. Natl. Acad. Sci.*, 105(17):6463–6468, 2008.

[22] Jason Ng, Alan H Kadish, and Jeffrey J Goldberger. Effect of electrogram characteristics on the relationship of dominant frequency to atrial activation rate in atrial fibrillation. *Heart Rhythm*, 3(11):1295–1305, 2006.

[23] Sandeep V Pandit and José Jalife. Rotors and the dynamics of cardiac fibrillation. *Circulation research*, 112(5):849–862, 2013.

[24] Stephan Rohr. Role of gap junctions in the propagation of the cardiac action potential. *Cardiovasc. Res.*, 62(2):309–322, 2004.

[25] Prashanthan Sanders, Omer Berenfeld, Mélèze Hocini, Pierre Jaïs, Ravi Vaidyanathan, Li-Fern Hsu, Stéphane Garrigue, Yoshihide Takahashi, Martin Rotter, Fréderic Sacher, et al. Spectral analysis identifies sites of high-frequency activity maintaining atrial fibrillation in humans. *Circulation*, 112(6):789–797, 2005.

[26] Robin M Shaw and Yoram Rudy. Ionic mechanisms of propagation in cardiac tissue roles of the sodium and l-type calcium currents during reduced excitability and decreased gap junction coupling. *Circ. Res.*, 81(5):727–741, 1997.

[27] Nicholas Sperelakis. An electric field mechanism for transmission of excitation between myocardial cells. *Circ. Res.*, 91(11):985–987, 2002.

[28] Nick Sperelakis and James E Mann. Evaluation of electric field changes in the cleft between excitable cells. *J. Theor. Biol*, 64(1):71–96, 1977.

[29] Kunichika Tsumoto, Takashi Ashihara, Narumi Naito, Takao Shimamoto, Akira Amano, Yasutaka Kurata, and Yoshihisa Kurachi. Specific decreasing of na+ channel expression on the lateral membrane of cardiomyocytes causes fatal arrhythmias in brugada syndrome. *Scientific reports*, 10(1):1–16, 2020.

[30] Dhananjay Vaidya, Houman S Tamaddon, Cecilia W Lo, Steven M Taffet, Mario Delmar, Gregory E Morley, and José Jalife. Null mutation of connexin43 causes slow propagation of ventricular activation in the late stages of mouse embryonic development. *Circ. Res.*, 88(11):1196–1202, 2001.

[31] Rengasayee Veeraraghavan, Joyce Lin, Gregory S Hoeker, James P Keener, Robert G Gourdie, and Steven Poelzing. Sodium channels in the cx43 gap junction perinexus may constitute a cardiac ephapse: an experimental and modeling study. *Pflügers Archiv-European Journal of Physiology*, 467(10):2093–2105, 2015.

[32] Atul Verma, Dhanunjaya Lakkireddy, Zaev Wulffhart, Jayasree Pillarisetti, Domenic Farina, Marianne Beardsall, Bonnie Whaley, David Giewercer, Bernice Tsang, and Yaariv Khaykin. Relationship between complex fractionated electrograms (cfe) and dominant frequency (df) sites and prospective assessment of adding df-guided ablation to pulmonary vein isolation in persistent atrial fibrillation (af). *Journal of cardiovascular electrophysiology*, 22(12):1309–1316, 2011.

[33] Ning Wei, Yoichiro Mori, and Elena G Tolkacheva. The dual effect of ephaptic coupling on cardiac conduction with heterogeneous expression of connexin 43. *J. Theor. Biol.*, 397:103–114, 2016.

[34] Ning Wei and Elena G Tolkacheva. Interplay between ephaptic coupling and complex geometry of border zone during acute myocardial ischemia: Effect on arrhythmogeneity. *Chaos: An Interdisciplinary Journal of Nonlinear Science*, 30(3):033111, 2020.

[35] Ning Wei and Elena G Tolkacheva. Mechanisms of arrhythmia termination during acute myocardial ischemia: Role of ephaptic coupling and complex geometry of border zone. *PloS one*, 17(3):e0264570, 2022.

[36] Fagen Xie, Zhilin Qu, Alan Garfinkel, and James N Weiss. Electrophysiological heterogeneity and stability of reentry in simulated cardiac tissue. *American Journal of Physiology-Heart and Circulatory Physiology*, 280(2):H535–H545, 2001.

[37] Jian-An Yao, David E Gutstein, Fangyu Liu, Glenn I Fishman, and Andrew L Wit. Cell coupling between ventricular myocyte pairs from connexin43-deficient murine hearts. *Circ. Res.*, 93(8):736–743, 2003.

[38] Kentaro Yoshida, Magnus Ulfarsson, Hakan Oral, Thomas Crawford, Eric Good, Krit Jongnarangsin, Frank Bogun, Frank Pelosi, Jose Jalife, Fred Morady, et al. Left atrial pressure and dominant frequency of atrial fibrillation in humans. *Heart rhythm*, 8(2):181–187, 2011.

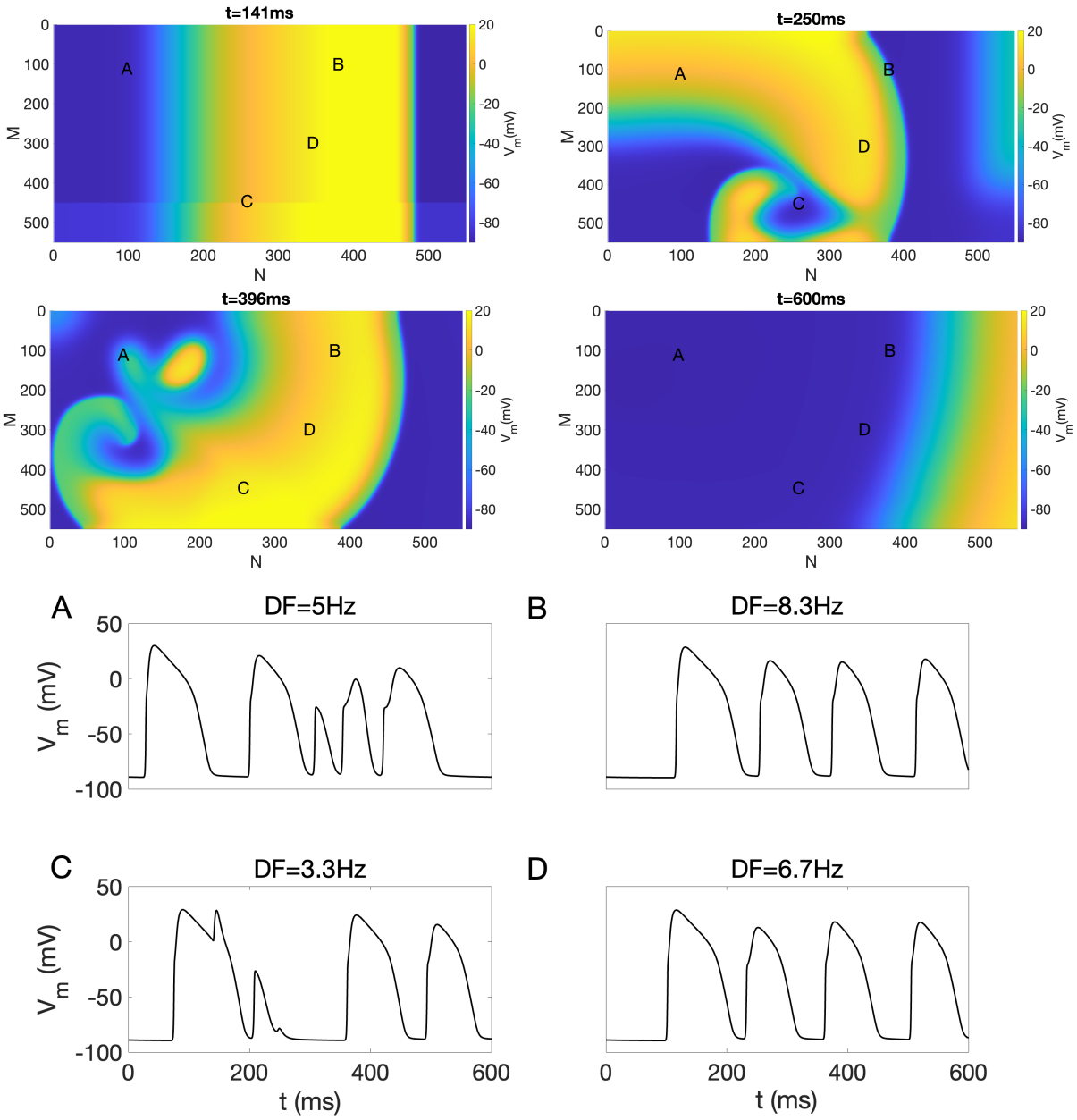

Figure 1: Top: Snapshots of nonsustained reentry in the presence of EpC at various time points (t) with $d_{\text{cleft}} = 15$ nm and 100% GJ. Bottom: Representative V_m traces for points A, B, C, and D, along with their corresponding DF values. The color bar shows the V_m values.

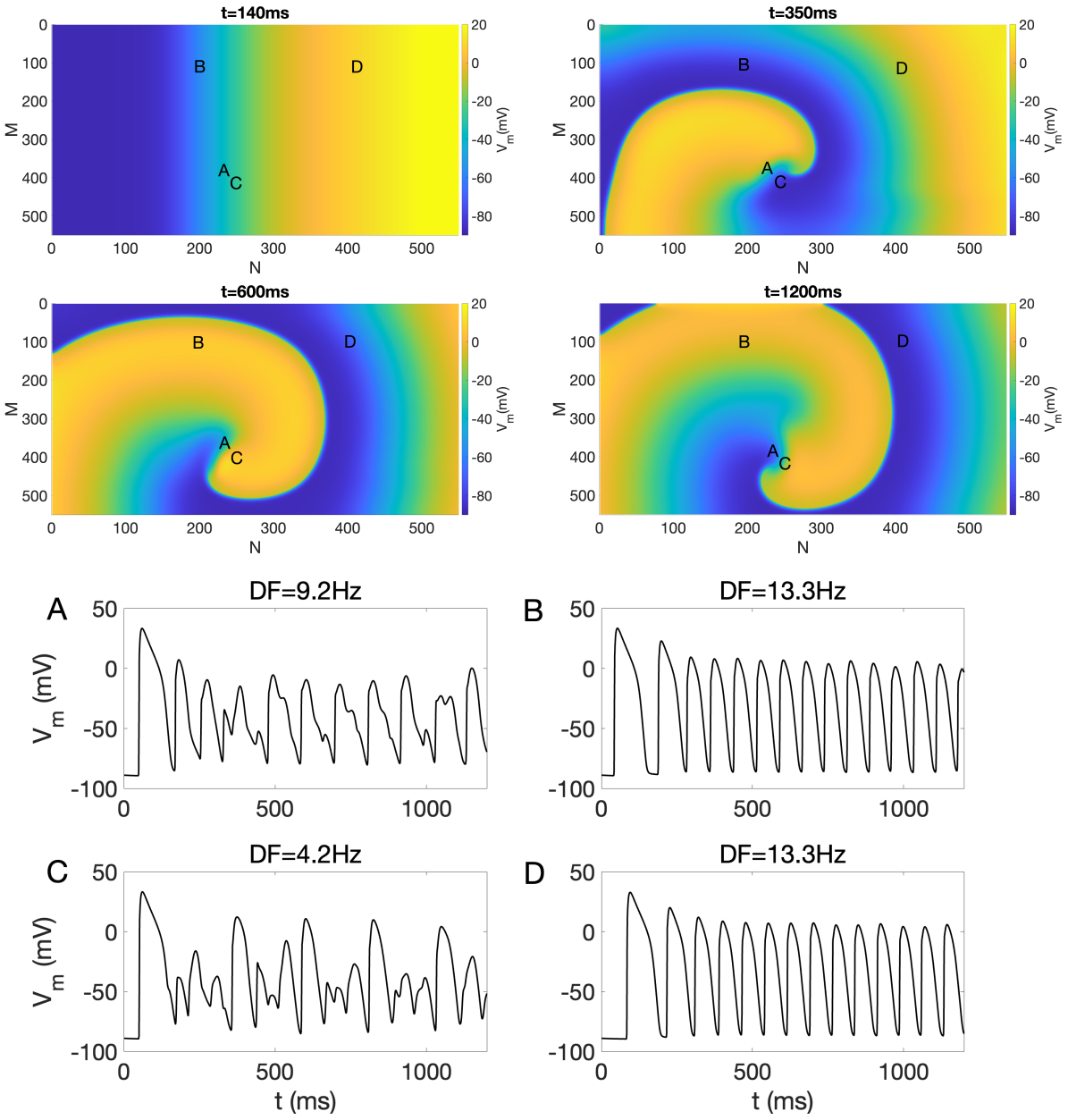

Figure 2: Top: Snapshots of sustained reentry in the near absence of EpC at various time points (t) with $d_{\text{cleft}} = 115$ nm and 100% GJ. Bottom: Representative V_m traces for points A, B, C, and D, along with their corresponding DF values. The color bar shows the V_m values.

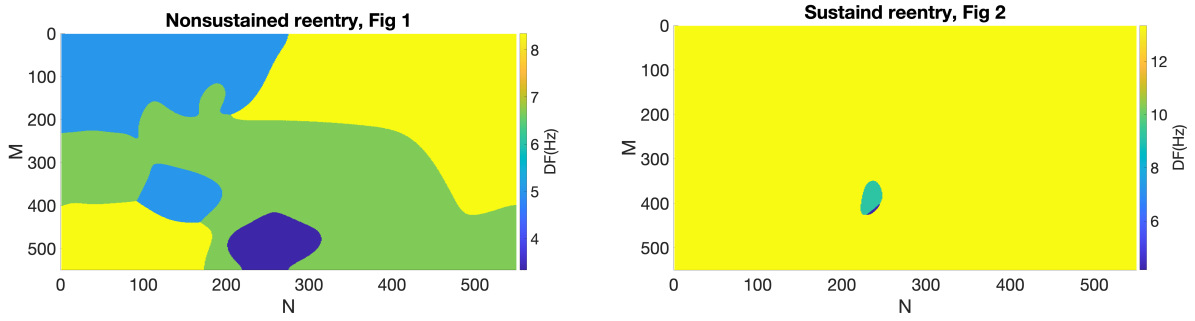

Figure 3: The 2D DF maps for nonsustained and sustained reentry shown in Figs. 1 and 2, respectively, at an S1-S2 interval of 140 ms.

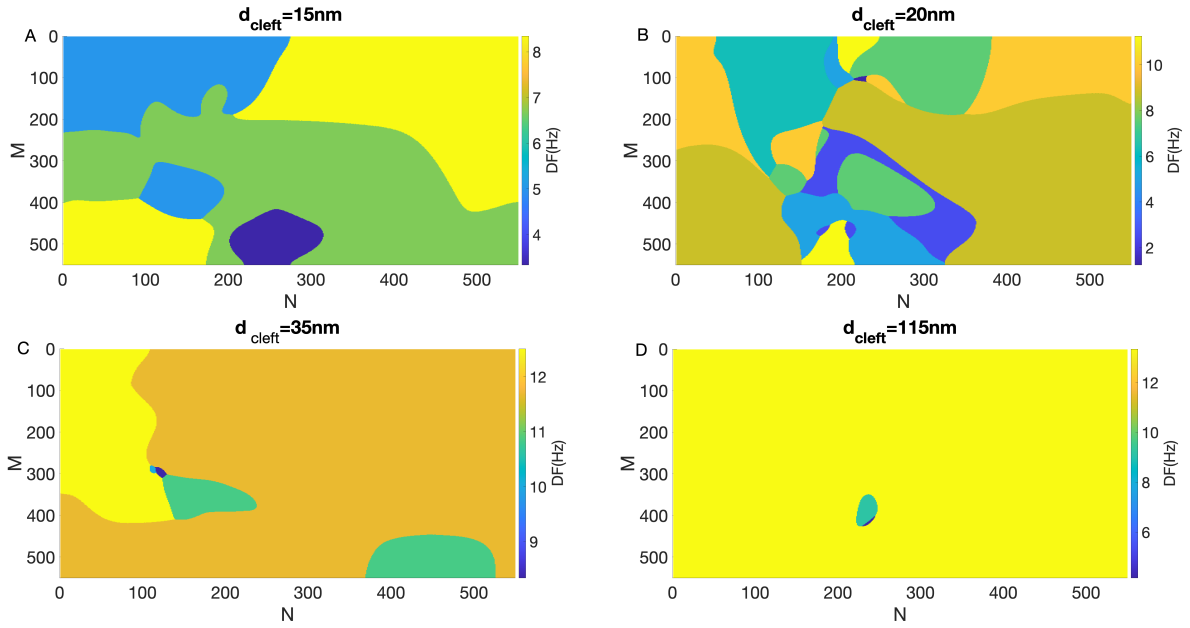

Figure 4: 2D DF maps for various d_{cleft} values (15 nm, 20 nm, 35 nm, and 115 nm in panels A–D) with 100% GJ. The colorbar indicates DF values (in Hz) derived from reentry at an S1-S2 interval of 140 ms.

GJ	Perturbation of initial condition	**EpC** (represented by d_{cleft} in nm)				
		8 nm	15 nm	20 nm	35 nm	115 nm
100%	-20%	Nonsustained	Nonsustained	Nonsustained	Sustained	Sustained
	-10%	Nonsustained	Nonsustained	Nonsustained	Sustained	Sustained
	0%	No	Nonsustained	Nonsustained	Sustained	Sustained
	+10%	No	Nonsustained	Sustained	Sustained	Sustained
	+20%	No	Nonsustained	Nonsustained	Sustained	Sustained
80%	-20%	Nonsustained	Nonsustained	Nonsustained	Sustained	Sustained
	-10%	Nonsustained	Nonsustained	Sustained	Sustained	Sustained
	0%	No	Nonsustained	Nonsustained	Sustained	Sustained
	+10%	No	Nonsustained	Sustained	Nonsustained	Sustained
	+20%	No	Nonsustained	Nonsustained	Sustained	Sustained
50%	-20%	Nonsustained	Nonsustained	Nonsustained	Sustained	Sustained
	-10%	Nonsustained	Sustained	Sustained	Sustained	Sustained
	0%	No	Nonsustained	Nonsustained	Nonsustained	Sustained
	+10%	No	Nonsustained	Sustained	Sustained	Sustained
	+20%	No	Nonsustained	Nonsustained	Sustained	Sustained
30%	-20%	Nonsustained	Nonsustained	Sustained	Sustained	Sustained
	-10%	Nonsustained	Nonsustained	Nonsustained	Sustained	Sustained
	0%	Nonsustained	Nonsustained	Sustained	Nonsustained	Sustained
	+10%	No	Nonsustained	Sustained	Sustained	Sustained
	+20%	No	Nonsustained	Nonsustained	Sustained	Sustained
10%	-20%	Sustained	Nonsustained	Sustained	Sustained	Sustained
	-10%	Nonsustained	Nonsustained	Nonsustained	Sustained	Sustained
	0%	Nonsustained	Nonsustained	Sustained	Sustained	Sustained
	+10%	No	Sustained	Sustained	Sustained	Sustained
	+20%	No	Nonsustained	Sustained	Sustained	Sustained

Table 1: Classification of reentry initiation: Outcomes are categorized as sustained (red), non-sustained (blue), or no reentry (black) across varying levels of GJs, EpC, and initial condition perturbations.

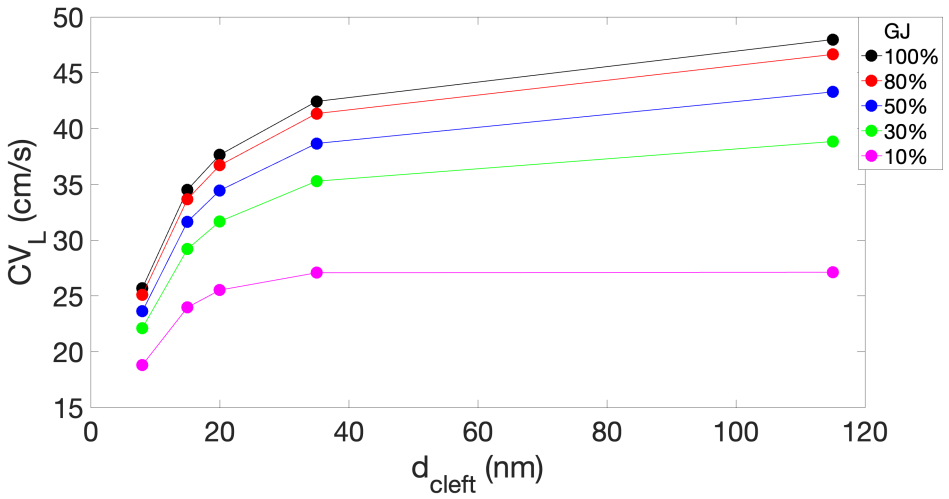

Figure 5: CV_L as a function of d_{cleft}, shown for various levels of GJs: 100% (black), 80% (red), 50% (blue), 30% (green), and 10% (magenta).

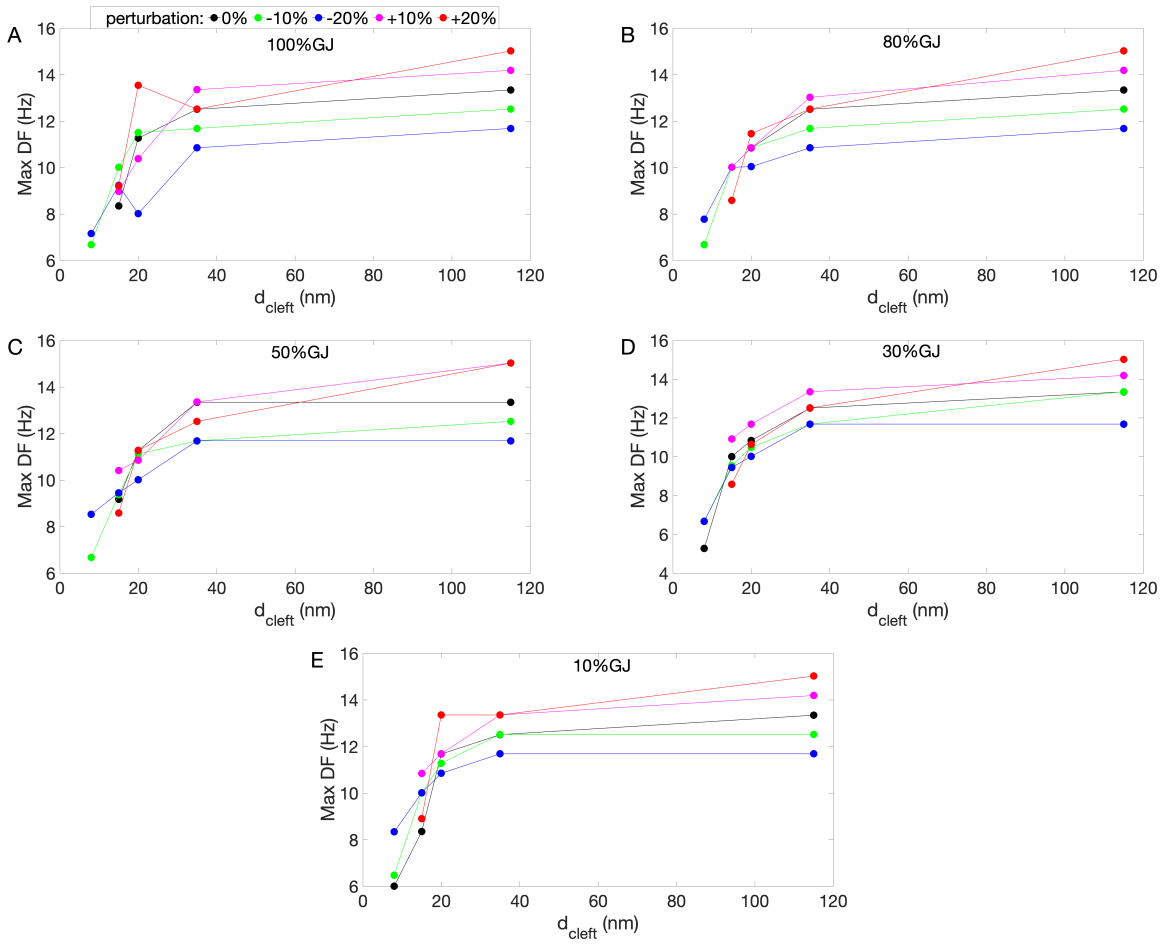

Figure 6: Max DF across varying levels of EpC (represented by d_{cleft}), GJs–100% (A), 80% (B), 50% (C), 30% (D), and 10% (E)–and initial condition perturbations: 0% (black), -10% (green), -20% (blue), +10% (magenta), and +20% (red). Results correspond to both nonsustained and sustained reentry summarized in Table 1.

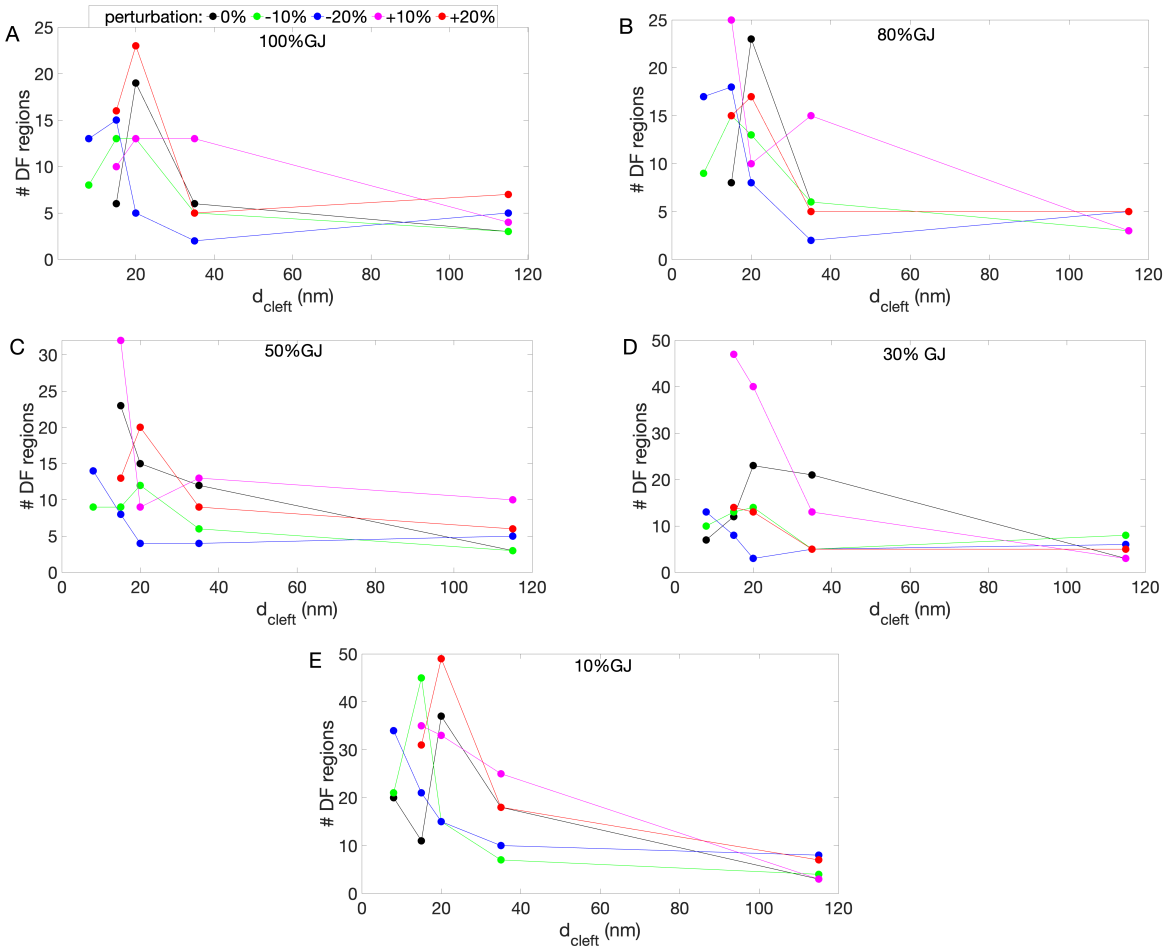

Figure 7: The # DF regions across varying levels of EpC (represented by d_{cleft}), GJs–100% (A), 80% (B), 50% (C), 30% (D), and 10% (E)–and initial condition perturbations: 0% (black), -10% (green), -20% (blue), +10% (magenta), and +20% (red). Results correspond to both nonsustained and sustained reentry summarized in Table 1.

GJ	**Perturbation of initial condition**	**EpC** (represented by d_{cleft} in nm)				
		8 nm	15 nm	20 nm	35 nm	115 nm
100%	-20%		Peak			
	-10%		Peak			
	0%			Peak		
	+10%			Peak		
	+20%			Peak		
80%	-20%		Peak			
	-10%		Peak			
	0%			Peak		
	+10%		Peak			
	+20%			Peak		
50%	-20%	Peak				
	-10%		Peak			
	0%		Peak			
	+10%		Peak			
	+20%			Peak		
30%	-20%	Peak				
	-10%			Peak		
	0%			Peak		
	+10%		Peak			
	+20%		Peak			
10%	-20%	Peak				
	-10%		Peak			
	0%			Peak		
	+10%		Peak			
	+20%			Peak		

Table 2: Identify the peaks of the # DF regions as a function of d_{cleft}, across varying levels of GJs and initial condition perturbations; peaks shown in red and blue indicate sustained and non-sustained reentry, respectively.